

This paper is a preprint of a paper accepted by IEE Proc. Vision, Image and Signal Processing and is subject to IEE Copyright. When the final version is published, the copy of record will be available at IEE Digital Library.

# Optimal Illumination for Three-Image Photometric Stereo using Sensitivity Analysis

A. D. Spence and M. J. Chantler

Texture Lab, School of Mathematical & Computer Sciences, Heriot-Watt University, Edinburgh, EH14 4AS, UK.  
Email: A.Spence@hw.ac.uk, M.J.Chantler@hw.ac.uk

**Abstract:** The optimal placement of the illumination for three-image photometric stereo acquisition of smooth and rough surface textures with respect to camera noise is derived and verified experimentally. The sensitivities of the scaled surface normal elements are derived and used to provide expressions for the noise variances. An overall figure of merit is developed by considering image-based rendering (i.e. relighting) of Lambertian surfaces. This metric is optimised numerically with respect to the illumination angles. An orthogonal configuration was found to be optimal. With regard to constant slant, the optimal separation between the tilt angles of successive illumination vectors was found to be  $120^\circ$ . The optimal slant angle was found to be  $90^\circ$  for smooth surface textures and  $55^\circ$  for rough surface textures.

## 1 Introduction

Photometric stereo [1] is an important technique for the acquisition, analysis and visualisation of surface texture. It uses three or more images captured from a single viewpoint of a surface illuminated from different directions to obtain descriptions of reflectance and relief. Its forte is in determining higher frequency surface information; the algorithm is less suited to determining global shape because it provides surface normal estimates which must be integrated to obtain height data. Woodham demonstrated that three images are sufficient for non-shadowed Lambertian surfaces [1]. The technique has been refined and modified to cope with non-Lambertian reflectance conditions such as shadows, specularities and interreflections [2,3,4,5,6,7]. However, the basic three-image algorithm is economical and often provides good results. It is also employed in more robust approaches e.g. 5-image photometric stereo in which the darkest and lightest pixels are discarded [2].

Illumination direction has a significant bearing on the accuracy of photometric stereo. Woodham advocates maximising the illumination slant angle for optimal performance [1] although he notes that its value is restricted in practice. This is due to the need to minimise the presence of shadows which are detrimental to performance. With regard to the relative position of the three light sources Woodham points out that a co-planar illumination arrangement

should be avoided [1]. Although the aforementioned guidelines are helpful, the illumination tilt angles which correspond to optimal performance have not been reported in the literature.

In this paper we use sensitivity analysis to derive an overall noise expression and then numerically minimise the function to determine the optimal illumination configuration for 3-image photometric stereo (PS). We verify the results empirically using thirty-one real textures. Each sample is ‘globally planar’ but has local surface variation. More precisely, the significant height variation is contained within the frequency range 5 cycles per image width up to the Nyquist frequency.

## 2 Three-Image Photometric Stereo

Assuming a point light source at infinity and ignoring shadowing and interreflections, an image pixel intensity corresponding to a facet of a Lambertian surface may be expressed as:

$$i(x, y) = \rho(x, y)\lambda\mathbf{l}\mathbf{n}(x, y) \quad (1)$$

where  $\rho(x, y)$  is the albedo,  $\mathbf{n}(x, y)$  is the surface normal,  $\lambda$  is the light source intensity and  $\mathbf{l}$  is the illumination vector.

We define  $\mathbf{l}$  in terms of slant angle  $\sigma$  and the tilt angle  $\tau$ . These parameters are equivalent to latitude and longitude respectively and can be measured for the light source position such that:

$$\mathbf{l} = (l_x, l_y, l_z) = (\cos \tau \sin \sigma, \sin \tau \sin \sigma, \cos \sigma) \quad (2)$$

Using three images taken under three different illumination vectors but from the same viewpoint provides:

$$\mathbf{i}(x, y) = \begin{bmatrix} i_1(x, y) \\ i_2(x, y) \\ i_3(x, y) \end{bmatrix} = \rho(x, y)\lambda \begin{bmatrix} \mathbf{l}_1 \\ \mathbf{l}_2 \\ \mathbf{l}_3 \end{bmatrix} \mathbf{n}(x, y) \quad (3)$$

This system of equations is sufficient to uniquely determine both the surface orientation  $\mathbf{n}$  and an albedo term  $\rho\lambda$  [1].

The illumination matrix  $(\mathbf{l}_1, \mathbf{l}_2, \mathbf{l}_3)^T$  in (3), which we now write as  $\mathbf{L}$ , can be inverted using singular value decomposition [17] to find:

$$\rho(x, y)\lambda\mathbf{n}(x, y) = \mathbf{s}(x, y) = \mathbf{L}^{-1}\mathbf{i}(x, y) \quad (4)$$

The product on the right-hand side of (4) is a vector which we define as the scaled surface normal  $\mathbf{s}(x, y) = [s_x(x, y) \ s_y(x, y) \ s_z(x, y)]^T$  for convenience. The albedo term is found from the magnitude of  $\mathbf{s}$  whilst the unit vector  $\mathbf{n}$  is determined by normalising it:

$$\rho(x, y)\lambda = \sqrt{s_x(x, y)^2 + s_y(x, y)^2 + s_z(x, y)^2} \quad (5)$$

$$\mathbf{n}(x, y) = \frac{\mathbf{s}(x, y)}{\sqrt{s_x(x, y)^2 + s_y(x, y)^2 + s_z(x, y)^2}} \quad (6)$$

It is straightforward to produce a bump map from the surface normal data thus acquired. The surface gradients  $p$  and  $q$  in the  $x$  and  $y$  directions respectively are given by:

$$p = -\frac{s_x(x, y)}{s_z(x, y)} \quad q = -\frac{s_y(x, y)}{s_z(x, y)} \quad (7,8)$$

An extra integration step using a technique such as that detailed in [18] is necessary to generate a corresponding height map.

### 2.1 Review of Accuracy Considerations

Accuracy is an issue which was considered by Woodham in some depth [1]. Reflectance maps, which are plots of intensity as a function of surface orientation in terms of the gradients  $p$  and  $q$ , were used to illustrate his main argument. He recommends dense iso-intensity contours for maximum accuracy. In this case a large change in intensity is attained for a small change in the surface gradient values  $p$  and  $q$ . In other words it is desirable to maximise  $\delta i/\delta p$  and  $\delta i/\delta q$ . Dense iso-intensity contours are achieved by increasing the value of the slant angle  $\sigma$  (see Fig. 1). In practice the slant angle is limited due to the adverse effect of the increasing presence of shadows as previously mentioned.

Apart from maximising the slant angle, recommendations for the relative position of the three light sources with regard to the tilt angle are not apparent in the literature. This issue is referred to indirectly by Woodham when he points out that the scheme cannot be solved when the illumination vectors are arranged in a co-planar configuration [1]. The resulting illumination matrix will be uninvertible in this case. For their two-image photometric stereo algorithm Lee and Kuo argue that the gradient direction of the reflectance map for one of the images should correspond to the tangential directions of the reflectance map of the other image [4]. They propose to achieve this by employing a difference of  $90^\circ$  between the illumination tilt angles. Gullón shows that the accuracy of her two-image techniques is more sensitive to tilt angle difference than the illumination arrangement position relative to a unidirectional surface and confirms that  $\Delta\tau=90^\circ$  is optimal [11]. With regard to using more than two lights with linear photometric stereo Gullón argues that an even arrangement is optimal since it maximises the linear term. The fact that side lighting acts as a directional filter of the surface height function suggests that the signal to noise ratio could be maximised by distributing the illumination tilt angles equally through  $360^\circ$  [10]. However, this has never been formally investigated with three-image photometric stereo. Lighting arrangements have been reported in the literature with regard to face recognition [19,20] but this work concerns the acquisition of images which can be directly employed as basis vectors for a linear sub-space and is not relevant to photometric stereo when only three input images are used.

## 3 Noise Expression Derivation

Sensitivity analysis is a common approach used to gain an insight into the behaviour of a mathematical model such as photometric stereo. It is the study of how the variation in the output of a model can be apportioned to different sources of variation [12]. In the case of photometric stereo, the output is the estimate of the surface orientation in the form of the scaled surface normal. We propose that ascertaining its response to variation in the input, namely the intensity images and their corresponding illumination conditions, would be useful in achieving our objective of determining optimal operating conditions. We note that Jiang and Bunke carried out a sensitivity analysis to examine the effect of measurement errors in the input data of photometric stereo but they did not consider the corresponding optimal illumination configuration [13]. Furthermore, we employ a different approach to effect the sensitivity analysis [8,9].

With regard to practical implementation, sensitivity analysis often takes the form of a sampling-based procedure during which the model is executed repeatedly over an extensive range of input conditions. We used this approach in order to produce empirical results and it will be discussed later. For a purely theoretical treatment, however, we derive expressions for the sensitivity of each scaled surface normal element  $s_x, s_y, s_z$  with respect to changes in the input image intensities  $i_1, i_2, i_3$ .

### 3.1 Sensitivity Analysis

When the illumination vectors are not constrained to be of common slant angle, the illumination matrix formed from them depends on six parameters. With tilt angles  $\tau_i$  and slant angles  $\sigma_i$  where  $i=1, 2, 3$ , the unit illumination vector matrix  $\mathbf{L}$  is:

$$\mathbf{L} = \begin{bmatrix} \cos \tau_1 \sin \sigma_1 & \sin \tau_1 \sin \sigma_1 & \cos \sigma_1 \\ \cos \tau_2 \sin \sigma_2 & \sin \tau_2 \sin \sigma_2 & \cos \sigma_2 \\ \cos \tau_3 \sin \sigma_3 & \sin \tau_3 \sin \sigma_3 & \cos \sigma_3 \end{bmatrix} \quad (9)$$

Substituting the inverse of  $\mathbf{L}$  into (4) provides expressions for each component of the scaled surface normal.

$$s_x = - \frac{\begin{pmatrix} (\sin \tau_3 \cos \sigma_2 \sin \sigma_3 - \sin \tau_2 \sin \sigma_2 \cos \sigma_3) i_1 \\ + (\sin \tau_1 \sin \sigma_1 \cos \sigma_3 - \sin \tau_3 \cos \sigma_1 \sin \sigma_3) i_2 \\ + (\sin \tau_2 \cos \sigma_1 \sin \sigma_2 - \sin \tau_1 \sin \sigma_1 \cos \sigma_2) i_3 \end{pmatrix}}{k_1} \quad (10)$$

$$s_y = - \frac{\begin{pmatrix} (\cos \tau_2 \sin \sigma_2 \cos \sigma_3 - \cos \tau_3 \cos \sigma_2 \sin \sigma_3) i_1 \\ + (\cos \tau_3 \cos \sigma_1 \sin \sigma_3 - \cos \tau_1 \sin \sigma_1 \cos \sigma_3) i_2 \\ + (\cos \tau_1 \sin \sigma_1 \cos \sigma_2 - \cos \tau_2 \cos \sigma_1 \sin \sigma_2) i_3 \end{pmatrix}}{k_1} \quad (11)$$

$$s_z = \frac{\begin{pmatrix} (\sin(\tau_3 - \tau_2) \sin \sigma_2 \sin \sigma_3) i_1 \\ + (\sin(\tau_1 - \tau_3) \sin \sigma_1 \sin \sigma_3) i_2 \\ + (\sin(\tau_2 - \tau_1) \sin \sigma_1 \sin \sigma_2) i_3 \end{pmatrix}}{k_1} \quad (12)$$

where

$$k_1 = \sin(\tau_3 - \tau_2) \cos \sigma_1 \sin \sigma_2 \sin \sigma_3 + \sin(\tau_1 - \tau_3) \sin \sigma_1 \cos \sigma_2 \sin \sigma_3 \\ + \sin(\tau_2 - \tau_1) \sin \sigma_1 \sin \sigma_2 \cos \sigma_3$$

Differentiating (10-12) with respect to each of the three image intensities gives nine sensitivity expressions. These describe how sensitive the error in the estimated components of the surface normal (compared to the true surface normal) is to error in the intensity measurements. We assume the latter to arise from sensor noise.

$$\frac{\partial s_x}{\partial i_1} = -\left(\frac{\sin \tau_3 \cos \sigma_2 \sin \sigma_3 - \sin \tau_2 \sin \sigma_2 \cos \sigma_3}{k_1}\right) \quad (13)$$

$$\frac{\partial s_y}{\partial i_1} = -\left(\frac{\cos \tau_2 \sin \sigma_2 \cos \sigma_3 - \cos \tau_3 \cos \sigma_2 \sin \sigma_3}{k_1}\right) \quad (14)$$

$$\frac{\partial s_z}{\partial i_1} = \left(\frac{\sin(\tau_3 - \tau_2) \sin \sigma_2 \sin \sigma_3}{k_1}\right) \quad (15)$$

$$\frac{\partial s_x}{\partial i_2} = -\left(\frac{\sin \tau_1 \sin \sigma_1 \cos \sigma_3 - \sin \tau_3 \cos \sigma_1 \sin \sigma_3}{k_1}\right) \quad (16)$$

$$\frac{\partial s_y}{\partial i_2} = -\left(\frac{\cos \tau_3 \cos \sigma_1 \sin \sigma_3 - \cos \tau_1 \sin \sigma_1 \cos \sigma_3}{k_1}\right) \quad (17)$$

$$\frac{\partial s_z}{\partial i_2} = \left(\frac{\sin(\tau_1 - \tau_3) \sin \sigma_1 \sin \sigma_3}{k_1}\right) \quad (18)$$

$$\frac{\partial s_x}{\partial i_3} = -\left(\frac{\sin \tau_2 \cos \sigma_1 \sin \sigma_2 - \sin \tau_1 \sin \sigma_1 \cos \sigma_2}{k_1}\right) \quad (19)$$

$$\frac{\partial s_y}{\partial i_3} = -\left(\frac{\cos \tau_1 \sin \sigma_1 \cos \sigma_2 - \cos \tau_2 \cos \sigma_1 \sin \sigma_2}{k_1}\right) \quad (20)$$

$$\frac{\partial s_z}{\partial i_3} = \left(\frac{\sin(\tau_2 - \tau_1) \sin \sigma_1 \sin \sigma_2}{k_1}\right) \quad (21)$$

As (4) is linear, the noise in the scaled surface normal  $\mathbf{s}$  can be simply derived from the sensitivities given by these equations. We note that the effect of inaccuracies in the measurement of the illumination angles is not considered here.

As mentioned, this was previously investigated and reported by Jiang et al [13].

### 3.2 Noise in the Scaled Surface Normal

If we assume that the noise in each image is Gaussian independent and of variance  $\overline{\psi}_i$  then the variance of the noise in  $s_x$  is given by:

$$\psi_{s_x} = \overline{\psi}_i \sqrt{\left(\frac{\partial s_x}{\partial i_1}\right)^2 + \left(\frac{\partial s_x}{\partial i_2}\right)^2 + \left(\frac{\partial s_x}{\partial i_3}\right)^2} \quad (22)$$

In order to allow a completely theoretical analysis the formulas were re-arranged to make them independent of input noise. A noise ratio is now predicted for each of the scaled surface normal elements. These expressions describe the error in the scaled surface normal relative to the average error in the input intensity measurements:

$$\frac{\psi_{s_x}}{\overline{\psi}_i} = \sqrt{\left(\frac{\partial s_x}{\partial i_1}\right)^2 + \left(\frac{\partial s_x}{\partial i_2}\right)^2 + \left(\frac{\partial s_x}{\partial i_3}\right)^2} \quad (23)$$

$$\frac{\psi_{s_y}}{\overline{\psi}_i} = \sqrt{\left(\frac{\partial s_y}{\partial i_1}\right)^2 + \left(\frac{\partial s_y}{\partial i_2}\right)^2 + \left(\frac{\partial s_y}{\partial i_3}\right)^2} \quad (24)$$

$$\frac{\psi_{s_z}}{\bar{\psi}_i} = \sqrt{\left(\frac{\partial s_z}{\partial i_1}\right)^2 + \left(\frac{\partial s_z}{\partial i_2}\right)^2 + \left(\frac{\partial s_z}{\partial i_3}\right)^2} \quad (25)$$

Substituting (13-21) into (23-25) gives the full equation for the noise ratio of each element in  $\mathbf{s}$ .

### 3.3 Single Figure of Merit

Given that noise is present in the input intensity images, it is apparent from the noise ratio expressions (23-25), once substituted with (13-21), that the resulting level of noise in the scaled surface normal estimates depends on the illumination configuration. Our objective is to establish operating conditions which minimise the noise in the output in order to determine accurate estimates of the surface normal. The optimal illumination configuration can therefore be found by minimising each of the three noise ratios. However, a single objective function is required in order to implement an optimisation procedure. It is possible to formulate such a metric by taking into account the intended use of the output data. We have chosen to consider image-based rendering applications. The intensity of a relit pixel under arbitrary illumination is given by Lambert's law (1); if re-written explicitly in terms of the scaled surface normal and illumination vector (2) it may be expressed as:

$$i(x, y) = s_x(x, y) \cos \tau \sin \sigma + s_y(x, y) \sin \tau \sin \sigma + s_z(x, y) \cos \sigma \quad (26)$$

Since the tilt and slant angles are specified in order to generate a relit image, the trigonometric terms in (26) reduce to scalars. Hence the relit intensity is simply a weighted sum of the elements of  $\mathbf{s}$ .

$$i(x, y) = k_x s_x(x, y) + k_y s_y(x, y) + k_z s_z(x, y) \quad (27)$$

We therefore choose our figure of merit to be the variance of the sum of the  $s_x$ ,  $s_y$  and  $s_z$  noise processes. We assume that these noise processes are highly correlated, each being a function of the three image noise processes. In this case the overall variance is simply given by the sum of the variances of the individual scaled surface normal elements. Our single figure of merit is hence given by the following equation.

$$M_{rough} = \frac{\psi_{s_x} + \psi_{s_y} + \psi_{s_z}}{\bar{\psi}_i} \quad (28)$$

Substituting (23-25) into (28) this becomes:

$$M_{rough} = \sqrt{\left(\frac{\partial s_x}{\partial i_1}\right)^2 + \left(\frac{\partial s_x}{\partial i_2}\right)^2 + \left(\frac{\partial s_x}{\partial i_3}\right)^2} + \sqrt{\left(\frac{\partial s_y}{\partial i_1}\right)^2 + \left(\frac{\partial s_y}{\partial i_2}\right)^2 + \left(\frac{\partial s_y}{\partial i_3}\right)^2} + \sqrt{\left(\frac{\partial s_z}{\partial i_1}\right)^2 + \left(\frac{\partial s_z}{\partial i_2}\right)^2 + \left(\frac{\partial s_z}{\partial i_3}\right)^2} \quad (29)$$

It is then straightforward to substitute (13-21) into (29) in order to provide the final expression. This is a function of illumination tilt and slant angles. Its form is ideally suited to an optimisation analysis. Minimising the equation to find the lowest value for the figure of merit will hence determine the optimal illumination configuration.

### 3.4 Smooth Surface Simplification

Whilst our approach does not take shadowing into account and is effectively independent of the distribution of surface normals, we may make an additional simplification for smooth surfaces. When the surface slope angles are less than  $15^\circ$  then the surface gradients  $p, q \ll 1$  and the term  $(p^2+q^2) < 0.1$  as noted in [14]. The implication is that since the surface normal may be expressed in terms of the gradients as follows:

$$\mathbf{n}(x, y) = \frac{[-p, -q, 1]^T}{\sqrt{p^2 + q^2 + 1}} \quad (30)$$

then the  $z$ -component of the scaled surface normal approximately equates to the local albedo term:

$$\begin{aligned} s_z(x, y) &= \rho(x, y) \lambda n_z(x, y) = \frac{\rho(x, y) \lambda}{\sqrt{p^2 + q^2 + 1}} \\ &\approx \rho(x, y) \lambda \quad \text{for } p, q \ll 1 \end{aligned} \quad (31)$$

Because  $s_z$  therefore tends to a constant in this case, it can be ignored for the purposes of a sensitivity analysis. The figure of merit for a smooth surface is therefore:

$$M_{smooth} = \frac{\psi_{s_x} + \psi_{s_y}}{\bar{\psi}_i} \quad (32)$$

Substituting (23,24) into (32) this becomes:

$$M_{smooth} = \sqrt{\left(\frac{\partial s_x}{\partial i_1}\right)^2 + \left(\frac{\partial s_x}{\partial i_2}\right)^2 + \left(\frac{\partial s_x}{\partial i_3}\right)^2} + \sqrt{\left(\frac{\partial s_y}{\partial i_1}\right)^2 + \left(\frac{\partial s_y}{\partial i_2}\right)^2 + \left(\frac{\partial s_y}{\partial i_3}\right)^2} \quad (33)$$

Substituting (13,14,16,17,19,20) into (33) provides an alternative figure of merit which specifically applies to smooth surfaces. This will allow the optimal behaviour of both types of surfaces to be compared and contrasted.

## 4 Empirical Determination of Noise

It is difficult to calculate the absolute noise in the photometric stereo process. However, the temporal noise in the process may be easily estimated for both input and output data. This facilitates an empirical investigation equivalent to the theoretical treatment detailed in the previous section.

With regard to data, images of a real isotropic texture (see texture  $m$ , Fig. 10) were acquired over a range of 86 illumination directions. A set of ten images was captured for each illumination direction. This meant that we could apply the photometric stereo algorithm ten times for a given illumination configuration. Temporal noise estimates corresponding to this configuration can be determined from the multiple input and output images. This is achieved by estimating the variance in the input intensity images and in the scaled surface normal elements.

### 4.1 Noise in the Input Intensity Images

Given ten  $n \times m$  images  $\mathbf{I}^t$  where  $t=1-10$  of the texture which correspond to a single illumination direction, a temporal noise value may be estimated from the mean of the per-pixel standard deviation of the intensity:

$$\psi_i = \frac{1}{mn} \sum_{x=1}^m \sum_{y=1}^n \sqrt{\frac{1}{9} \sum_{t=1}^{10} (i^t(x, y) - \bar{i}(x, y))^2} \quad (34)$$

$$\text{where } \bar{i}(x, y) = \frac{1}{10} \sum_{t=1}^{10} i^t(x, y)$$

Since there are three illumination directions in the input data, three temporal noise values  $\psi_{i_1}, \psi_{i_2}, \psi_{i_3}$  are calculated using (34). A mean value for the input noise is determined as follows:

$$\bar{\psi}_i = \frac{\psi_{i_1} + \psi_{i_2} + \psi_{i_3}}{3} \quad (35)$$

#### 4.2 Noise in the Scaled Surface Normal Element

Given ten  $n \times m$  images  $\mathbf{S}^t$  where  $t=1-10$  of a scaled surface normal element estimate which correspond to a given illumination configuration, a mean temporal noise value is similarly estimated from the mean of the per-pixel standard deviation:

$$\psi_s = \frac{1}{mn} \sum_{x=1}^m \sum_{y=1}^n \sqrt{\frac{1}{9} \sum_{t=1}^{10} (s^t(x, y) - \bar{s}(x, y))^2} \quad (36)$$

$$\text{where } \bar{s}(x, y) = \frac{1}{10} \sum_{t=1}^{10} s^t(x, y)$$

Since there are three scaled surface normal  $\psi_{s_x}, \psi_{s_y}, \psi_{s_z}$  elements, three temporal noise values are generated.

#### 4.3 Figure of Merit

Empirical estimates of the figures of merit for rough and smooth surfaces  $M_{rough}$  and  $M_{smooth}$  are calculated with (28,32) using the temporal noise estimates  $\bar{\psi}_i, \psi_{s_x}, \psi_{s_y}, \psi_{s_z}$ .

### 5 Investigation into Optimal Performance

The figures of merit enabled us to undertake an investigation into the performance of the three-image photometric stereo technique with a view to determining the optimal illumination configuration. We estimated theoretical and empirical values for  $M_{rough}$  and  $M_{smooth}$  for a series of illumination configurations. In one type of experiment we varied the illumination tilt angle corresponding to the third input image. In a second type of experiment we varied the illumination slant angle common to all three images. The results are presented graphically in the following sub-section. Later in this section we consider the numerical minimisation of the theoretical expressions.

## 5.1 Graphical Representation

Here we consider three input images which have corresponding illumination tilt angles of  $\tau_1$ ,  $\tau_2$ ,  $\tau_3$  and a common slant angle  $\sigma$ .

### 5.1.1 Tilt Angle $\tau_3$ Variation

In these experiments the tilt angles  $\tau_1$  and  $\tau_2$  and the common slant angle  $\sigma$  were held constant. Their values were chosen to correspond to illumination configurations which are typically employed in photometric stereo. In one set of experiments we used  $\tau_1 = 0^\circ$ ,  $\tau_2 = 90^\circ$ ,  $\sigma = 45^\circ$  and in another we used  $\tau_1 = 0^\circ$ ,  $\tau_2 = 120^\circ$ ,  $\sigma = 45^\circ$ . Both sets of experiments involved altering the illumination configuration by varying the third tilt angle  $\tau_3$  (see Fig. 2). With regard to the images of the real texture, its value was increased by  $10^\circ$  increments over a complete tilt angle rotation ( $0^\circ \leq \tau_3 < 360^\circ$ ,  $\Delta\tau_3 = 10^\circ$ ). With regard to the theoretical approach we used increments of  $1^\circ$  ( $\Delta\tau_3 = 1^\circ$ ).

Figure of merit values were estimated for each configuration. Typical plots are given in Fig. 3 & 4. A noticeable feature common to both graphs is that the noise ratio goes off the scale as the third tilt angle coincides with values corresponding to the first and second angles. This is the co-planar situation when the inverse of the illumination matrix does not exist. In this instance it is not possible to solve the system of equations for the unknowns. It is also apparent that increases in the value of the figure of merit become more significant as this situation is approached.

The most interesting feature common to both graphs is that there exists a third tilt angle which corresponds to a minimum. This is approximately  $240^\circ$  when the first and second tilt angles are set to  $0^\circ$  and  $120^\circ$  respectively as highlighted on the plot. However, if these angles are changed to  $0^\circ$  and  $90^\circ$  the optimal third tilt angle is not  $180^\circ$  but around  $225^\circ$ . This means that McGunnigle's photometric scheme [15] is sub-optimal but not significantly so and has the advantage of being straightforward to solve.

### 5.1.2 Slant Angle $\sigma$ Variation

In these experiments the three tilt angles  $\tau_1$ ,  $\tau_2$ ,  $\tau_3$  were held constant. In the set of experiments presented here we used the optimal values  $\tau_1 = 0^\circ$ ,  $\tau_2 = 120^\circ$ ,  $\tau_3 = 240^\circ$  determined for a common illumination slant angle configuration. The experiments involved altering the illumination configuration by varying the value of the common slant angle  $\sigma$  (see Fig. 5) where  $\sigma = \sigma_1 = \sigma_2 = \sigma_3$ . With regard to the images of the real texture, its value was increased in increments of  $5^\circ$  for a range of slant angles ( $20^\circ \leq \sigma \leq 70^\circ$  with  $\Delta\sigma = 5^\circ$ ). With regard to the theoretical approach we used increments of  $1^\circ$  ( $\Delta\sigma = 1^\circ$ ). Figure of merit values were estimated for each configuration.

In this case it is actually the difference in behaviour between the two kinds of surfaces which is interesting. Plots of the figures of merit for rough and smooth surfaces are presented in Fig. 6 & 7. Fig. 6 demonstrates that with regard to minimising our figure of merit for a texture of rough surface, a slant angle of about  $55^\circ$  is optimal. However, different behaviour is observed for a smooth surface (Fig. 7). The minimum no longer corresponds to  $55^\circ$  but has increased

beyond the range of the graph. Extrapolation appears to suggest that in this case a slant angle of 90° is optimal. This observation will be confirmed by minimisation in the following section.

## 5.2 Minimisation

The plot profiles given in the previous section each indicate a minimum noise ratio with regard to both tilt and slant angle. An optimisation procedure was used to precisely determine the corresponding parameter values. The figure of merit formulas were numerically minimised by application of the Nelder-Mead algorithm [16]. This approach facilitated an investigation into the existence of a global minimum.

### 5.2.1 Four Parameter Minimisation

This minimisation procedure yields the value of three tilt angles and a common slant angle (see Table 1 & 2). The minimum value of the figure of merit was not found to correspond to unique values for the tilt angles but to a unique difference in tilt angle of 120°. This is true for both rough and smooth surfaces. It also agrees with the observation from Fig. 3. With regard to the slant angle, a unique value of approximately 54.7° is apparent for rough surfaces (see Table 1). This value increases to 90° for smooth surfaces (see Table 2) although this result is not of practical value since in reality light from a source in this position would not impinge on the surface.

Table 1: Examples of 4-parameter minimisation results for a rough surface

$M_{rough}$	$\tau_1$	$\tau_2$	$\tau_3$	$\sigma$
3.0	0.0°	120.0°	240.0°	54.7°
3.0	176.4°	56.4°	296.4°	54.7°
3.0	324.4°	84.4°	204.4°	54.7°

Table 2: Examples of 4-parameter minimisation results for a smooth surface

$M_{smooth}$	$\tau_1$	$\tau_2$	$\tau_3$	$\sigma$
1.6	0.0°	120.0°	240.0°	90.0°
1.6	272.1°	32.1°	152.1°	90.0°
1.6	63.8°	303.8°	183.8°	90.0°

The marked difference in the optimal slant angle for rough and smooth surfaces cannot be attributed to shadowing since our approach does not take it into account. The results can be explained by considering the difference between the two figures of merit, namely the noise ratio for the  $z$ -component of the scaled surface normal. In this simplified case of common slant angle, expressions for each element of the scaled surface normals (10-12) simplify to the following:

$$s_x = -\left( \frac{(\sin \tau_3 - \sin \tau_2)i_1 + (\sin \tau_1 - \sin \tau_3)i_2 + (\sin \tau_2 - \sin \tau_1)i_3}{k_2 \sin \sigma} \right) \quad (37)$$

$$s_y = -\left( \frac{(\cos \tau_2 - \cos \tau_3)i_1 + (\cos \tau_3 - \cos \tau_1)i_2 + (\cos \tau_1 - \cos \tau_2)i_3}{k_2 \sin \sigma} \right) \quad (38)$$

$$s_z = \left( \frac{\sin(\tau_3 - \tau_2)i_1 + \sin(\tau_1 - \tau_3)i_2 + \sin(\tau_2 - \tau_1)i_3}{k_2 \cos \sigma} \right) \quad (39)$$

where  $k_2 = \sin(\tau_3 - \tau_2) + \sin(\tau_1 - \tau_3) + \sin(\tau_2 - \tau_1)$

The denominator of the  $z$ -component of the scaled surface normal (39) and therefore that of the respective sensitivities contains  $\cos \sigma$  whilst that for the  $x$  and  $y$  components (37,38) has  $\sin \sigma$ . Since the  $z$ -component is omitted for a smooth surface, a maximum slant results in a minimum  $M_{smooth}$ .

We note that the angles determined for the rough surface in Table 1 mean that the corresponding optimal illumination vectors are orthogonal.

### 5.2.2 Six Parameter Minimisation

The minimisation was also performed in a completely unconstrained manner such that the slant angles were no longer required to be common to the three illumination directions. The examples given in Table 3 demonstrate that the conditions corresponding to the minimum noise ratio are not in fact unique but depend on the initial conditions specified in every optimisation. However, in each case the three resulting illumination vectors are orthogonal.

Table 3: Examples of 6-parameter minimisation results for a rough surface

$M_{rough}$	$\tau_1$	$\tau_2$	$\tau_3$	$\sigma_1$	$\sigma_2$	$\sigma_3$
	0.0°	112.4°	239.4°	55.3°	56.1°	48.2°
3.0	13.9°	135.0°	255.6°	55.3°	53.3°	55.6°
	70.5°	189.4°	315.3°	59.4°	50.8°	54.3°

To help illustrate this result, we plotted  $M_{rough}$  against the dot products of pairs of illumination vectors (see Fig. 8). The minimum of the data cloud corresponds to dot products of zero and hence optimal performance corresponds to an orthogonal illumination configuration.

### 5.3 Summary of Findings

With regard to three-image Lambertian photometric stereo we found that the optimal illumination configuration cannot be specified in terms of a unique set of values for the tilt and slant angles defining illumination direction. Instead we determined that the optimal operating conditions correspond to an orthogonal configuration i.e. when the three illumination vectors are at an angle of 90° to each other (see Fig. 9).

The use of an orthogonal configuration may not be practicable unless the illumination slant angles are constrained to take a common value. In this case the use of a 120° difference in tilt angle is to be recommended. This was found to be applicable to both rough and smooth surfaces. When shadowing is not an issue and the surface is rough in character, a slant angle of around 55° can be used to attain optimal operating conditions. If shadowing is present then this value should be reduced. If on the other hand the surface can be considered to be smooth in nature and not susceptible to shadows then this value can be increased. In this case the term ‘grazing’ can be used to describe the resulting illumination conditions.

## 6 Practical Assessment

The recommendations for optimal placement of the lights presented in the previous section minimise the effect of camera noise but assume that the surfaces are Lambertian and that there are no shadows. The validity of the proposed illumination conditions is hence uncertain for the non-ideal case. A quantitative assessment of a practical nature was therefore undertaken to investigate this issue. This involved the use of thirty-one real textures many of which are prone to non-ideal reflectance characteristics such as shadowing and specular highlights (see Fig. 10). Images of the textures corresponding to a variety of illumination configurations were processed using the three-image photometric stereo algorithm. The Lambertian model (1) was then used to relight the generated surface gradient and albedo images.

### 6.1 Relighting Assessment

The relit images produced were then compared to the originals but not just visually; the difference between them was quantitatively measured. We used a signal to relight error ratio  $SE_R$  as a measure of the difference in intensity values between an original image and a corresponding relit image:

$$SE_R(j) = 10 \log \left[ \frac{\text{var}[\mathbf{I}(\tau_j, \sigma_j)]}{\text{var}[\mathbf{I}(\tau_j, \sigma_j) - \mathbf{I}_{relight}(\tau_j, \sigma_j)]} \right] \quad (40)$$

where  $\mathbf{I}(\tau_j, \sigma_j)$  is a data set image,  $\mathbf{I}_{relight}(\tau_j, \sigma_j)$  is the corresponding generated image relit under the  $j^{\text{th}}$  illumination direction defined by the tilt angle  $\tau_j$  and slant angle  $\sigma_j$  and  $\text{var}[\mathbf{I}]$  is the variance of the intensity image.

We obtained an estimate of the overall relight accuracy for each texture by calculating  $SE_R$  values for a series of relit images and taking their mean. The texture signal to relight error ratio  $TSE_R$  is hence given by:

$$TSE_R_{tx} = \frac{1}{n} \sum_{j=1}^n [SE_R_{tx}(j)] \quad (41)$$

for a texture  $tx$  where  $n$  is the number of original-relit image pairs considered. In order to avoid bias, we note that the relit images used to calculate the  $TSE_R$  should be estimates of images in the database which have not been used as input data.

A visual inspection of the relight error was also provided through the use of difference images. These are generated by subtracting the relit image from its corresponding data set image and taking the magnitude of the result i.e.  $|\mathbf{I}(\tau, \sigma) - \mathbf{I}_{relight}(\tau, \sigma)|$ . This implies that relatively accurate regions will be dark and relatively inaccurate regions will be light.

### 6.2 Tilt Angle Spacing

Three different tilt angle spacings were utilised in the experiments. These correspond to the theoretical optimal ( $\Delta\tau=120^\circ$ ), McGunnigle's simplified photometric scheme ( $\Delta\tau=90^\circ$ ) and finally an asymmetric arrangement ( $\Delta\tau=50^\circ$ ). A constant slant angle of  $45^\circ$  was used in every case. Following each application of the algorithm relit images were generated over a complete revolution in terms of tilt angle ( $\Delta\tau=10^\circ$ ) for the two other slant angle values present in the image database i.e.  $\sigma=30^\circ$  and  $60^\circ$ . This avoided the case when the illumination conditions of a relit image correspond to that of an input image when the relight error would tend towards zero. For each texture the *SER* was estimated for each of the 72 illumination directions using (40). A value for the *TSER* was then obtained from (41). This was calculated for each of the three tilt angle spacings with every texture. The results are presented in the bar chart in Fig. 11.

Whilst it is evident that some of the textures are more suited to use with Lambertian photometric stereo than others, it is apparent that the proposed optimal illumination arrangement has outperformed the other arrangements in all but one case. The exception (texture *ac*) relates to a specular texture with less than ideal reflection. The tilt angle spacing of  $90^\circ$  performs well but the resulting *TSER* values are relatively low in general compared to the optimal case. The asymmetric case performs poorly in comparison. This is also apparent from the samples of relit images given in Fig. 12 on comparison with the original image. Again it is clear that the optimal configuration provides a consistently better approximation to the original intensity image.

We conclude that the optimal spacing of the illumination vectors is  $120^\circ$  with regard to tilt angle when they are constrained to be of common slant angle and that there is a benefit in terms of accuracy when this configuration is utilised on a practical basis.

### 6.3 Slant Angle Selection

Experiments concerning the slant angle were also undertaken. In this case illumination configurations using the optimal tilt angle spacing of  $120^\circ$  were used with a range of slant angles common to each illumination vector ( $30^\circ \leq \sigma \leq 60^\circ$  with  $\Delta\sigma=15^\circ$ ). Following each application of the algorithm relit images were generated over a complete revolution in terms of tilt angle ( $\Delta\tau=10^\circ$ ) for the two other slant angle values. For example, if the input images illumination slant angle is  $30^\circ$  then 72 relit images would be generated with slant angles of  $45^\circ$  and  $60^\circ$ . Whilst this approach is not ideal it provides some insight into the issue of slant angle selection which is potentially dependent on the surface type according to the theory and is furthermore constrained by the need to minimise the presence of shadows. The results are presented in Fig. 13.

Assuming that the comparison is valid, it is evident that in general it is preferable to use a slant angle of  $45^\circ$  because this intermediate value corresponds to the best performance of photometric stereo for the majority of real textures. This result merely helps to confirm that the effect of shadowing is important. It is not really possible to distinguish between

our proposed optimal value of around  $55^\circ$  for rough surface texture and Woodham's recommendation of maximising slant angle because of the impact of shadowing for larger slant angles. Shadowing is not taken into consideration in either of the theoretical evaluations. However, based on evidence from these practical results for thirty-one textures it is prudent to avoid the use of extreme slant values. Overall a value of  $45^\circ$  appears to be more appropriate for textures of a similar nature to that used in the investigation.

#### 6.4 Discussion

Whilst the optimal illumination conditions proposed in this paper are potentially useful on a practical basis, we note that they have been derived for a texture exhibiting ideal diffuse reflection. The fact that neither shadows, specularities nor interreflections have been considered in the development of the theory means that the application of such guidelines should really be restricted. However, the assessment of the three-image photometric stereo technique with real textures demonstrated that even in the presence of shadows and specularities, using the  $120^\circ$  tilt angle spacing with constant slant angle was in fact relatively beneficial. In the case of specular reflectance this may well be because the specular peak is narrow and therefore not frequently observed under the three light positions. For textures which exhibit far from ideal reflectance the recommended illumination arrangement can simply be used as a first guess of optimal illumination conditions.

## 7 Conclusions

Overall, we conclude that a difference between successive tilt angles of  $120^\circ$  is to be recommended when the illumination configuration is constrained to have a common slant angle. Based on the theoretical and empirical evidence presented we recommend the use of a maximum slant angle of  $55^\circ$  for rough surface textures.

## References

- 1 Woodham, R. J.: 'Photometric method for determining surface orientation from multiple images', *Optical Engineering*, 1980, **19**(1), pp. 139-144
- 2 Rushmeier, H., Taubin, G., and A. Guezic: 'Applying shape from lighting variation to bump map capture', in *Proceedings of Eurographics Rendering Workshop 1997*, pp. 35 –44
- 3 Coleman, E. N., Jain, R.: 'Obtaining 3-dimensional shape of textured and specular surfaces using four-source photometry', *Computer Graphics and Image Processing*, 1982, **18**, pp.309-328
- 4 Lee, K.M. and Kuo, C.C.J.: 'Surface reconstruction from photometric stereo images', *Journal of the Optical Society of America A*, 1993, **10**(5), pp. 855-868
- 5 Yamada, T., Saito, H. and Ozawa, S.: '3D reconstruction of skin surface from image sequence', in *Proceedings of MVA98: Workshop of Machine Vision Applications*, 1998, pp.384-387

- 6 Hansson, P. and Johansson, P.-Å.: 'Topography and reflectance analysis of paper surfaces using a photometric stereo method', *Optical Engineering*, 2000, **39**(9), pp.2555-2561
- 7 Schlüns, K.: 'Shading based 3D shape recovery in the presence of shadows', in *Proceedings of the First Joint Australia & New Zealand Biennial Conference on Digital Image & Vision Computing: Techniques and Applications*, 1997, pp. 195-200
- 8 Spence, A.D. and Chantler, M.J.: 'Optimal illumination for three-image photometric stereo acquisition of surface texture', in *Proceedings of the 3<sup>rd</sup> International Workshop on Texture Analysis and Synthesis*, 2003, pp. 89-94
- 9 Spence, A.D.: 'Calibrated and Uncalibrated Photometric Stereo for Surface Texture Acquisition', *Ph.D. thesis*, 2005, School of Mathematical and Computer Sciences, Heriot-Watt University
- 10 Chantler, M. J.: 'Why illuminant direction is fundamental to texture analysis', *IEE Proceedings Vision, Image and Signal Processing*, 1995, **142**(4), pp.199-206
- 11 Gullón, C.: 'Height recovery of rough surfaces from intensity images', *Ph.D. thesis*, 2002, School of Engineering and Physical Sciences, Heriot-Watt University
- 12 Saltelli, A., Chan, K. and Scott, E.M.: 'Sensitivity analysis', 2000, Wiley.
- 13 Jiang, X.Y. and Bunke, H.: 'On error analysis for surface normals determined by photometric stereo', *Signal Processing*, 1991, **23**, pp. 221-226
- 14 Kube, P. and Pentland, A.: 'On the imaging of fractal surfaces', *IEEE Transactions on Pattern Analysis and Machine Intelligence*, 1988, **10**(5), pp.704-707
- 15 McGunnigle, G.: 'The classification of texture surfaces under varying illumination direction', *Ph.D. thesis*, 1998, Dept. of Computing and Electrical Engineering, Heriot-Watt University.
- 16 Nelder, J.A. and Mead, R.: 'A simplex method for function minimisation', *Computer Journal*, 1965, **7**(4), pp.308-313
- 17 Press, W.H., Flannery, B.P., Teukolsky S.A. and Vetterling, W.T.: 'Numerical recipes in C' (Cambridge University Press, 1988)
- 18 Frankot, R.T. and Chellappa, R.: 'A method for enforcing integrability in shape from shading algorithms', *IEEE Transactions on Pattern Analysis and Machine Intelligence*, July 1988, **10**(4)
- 19 Lee, K., Ho, J. and Kriegman, D.: 'Nine points of light: acquiring subspaces for face recognition under variable lighting', in *Proceedings of IEEE Conference on Computer Vision and Pattern Recognition*, 2001, pp.519-526
- 20 Lee, K., Ho, J. and Kriegman, D.: 'Acquiring linear subspaces for face recognition under variable lighting', *IEEE Transactions on Pattern Analysis and Machine Intelligence*, May 2005, **27**(5), pp.684 - 698

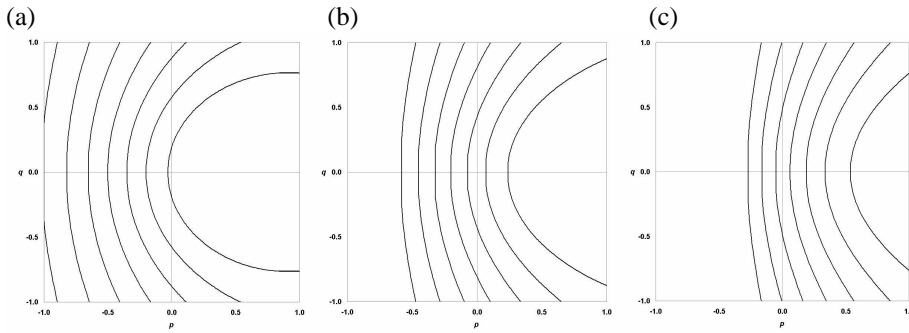


Fig. 1 Reflectance maps for a Lambertian surface with illumination slant angle  $\sigma$  (a)  $30^\circ$ , (b)  $45^\circ$ , (c)  $60^\circ$  and  $\tau=0^\circ$ .

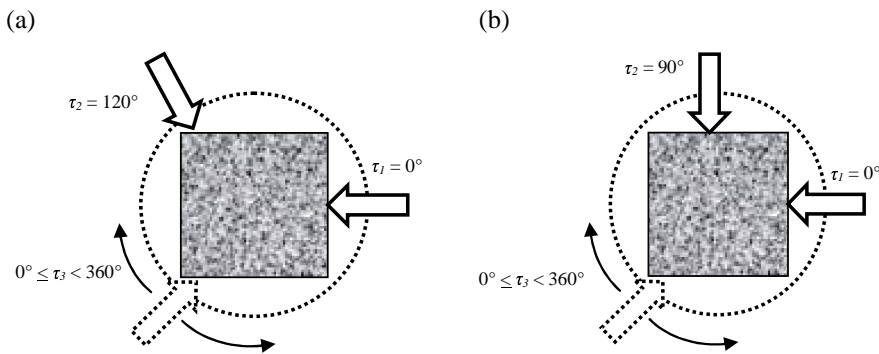


Fig. 2 Example of range of illumination configurations for two tilt angle experiments (Plan view). Increments are  $\Delta\tau_3 = 1^\circ$  (theoretical),  $\Delta\tau_3 = 10^\circ$  (empirical).

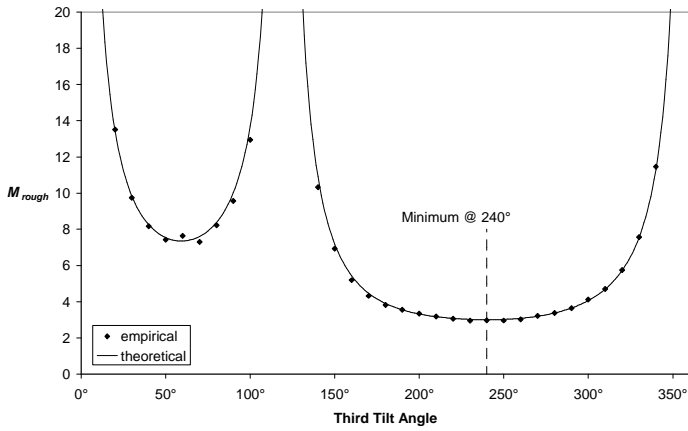


Fig. 3 Figure of merit  $M_{rough}$  versus third tilt angle  $\tau_3$  with  $\tau_1=0^\circ$ ,  $\tau_2=120^\circ$ .

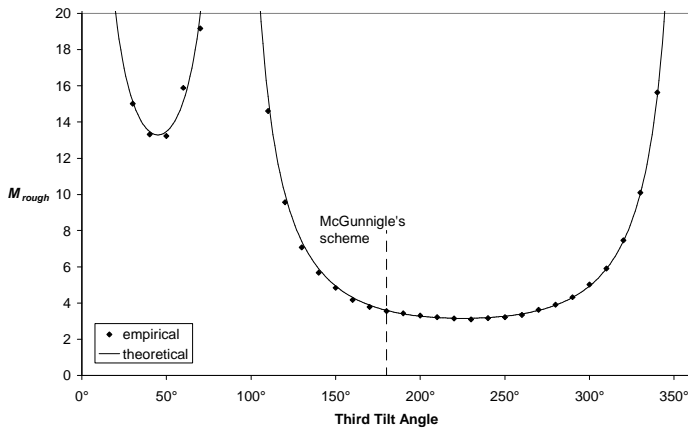


Fig. 4 Figure of merit  $M_{rough}$  versus third tilt angle  $\tau_3$  with  $\tau_1=0^\circ$ ,  $\tau_2=90^\circ$ .

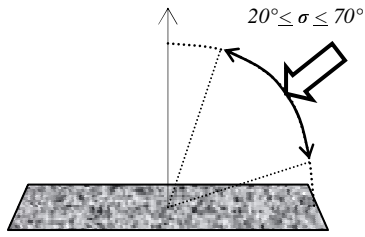


Fig. 5 Illustration of range of illumination slant angles in experiments. Increments are  $\Delta\sigma = 1^\circ$  (theoretical),  $\Delta\sigma = 5^\circ$  (empirical).

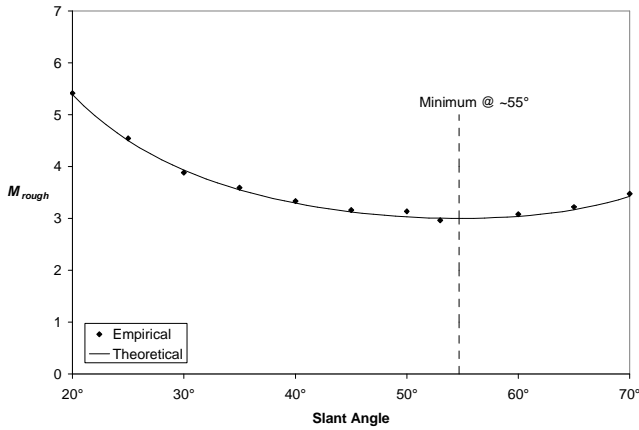


Fig. 6 Total noise ratio  $M_{rough}$  versus slant angle  $\sigma$  with  $\tau_1=0^\circ$ ,  $\tau_2=120^\circ$ ,  $\tau_3=240^\circ$ .

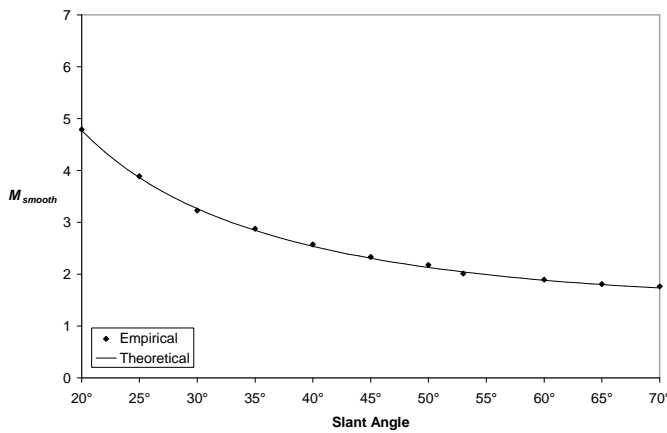


Fig. 7 Total noise ratio  $M_{smooth}$  versus slant angle  $\sigma$  with  $\tau_1=0^\circ$ ,  $\tau_2=120^\circ$ ,  $\tau_3=240^\circ$ .

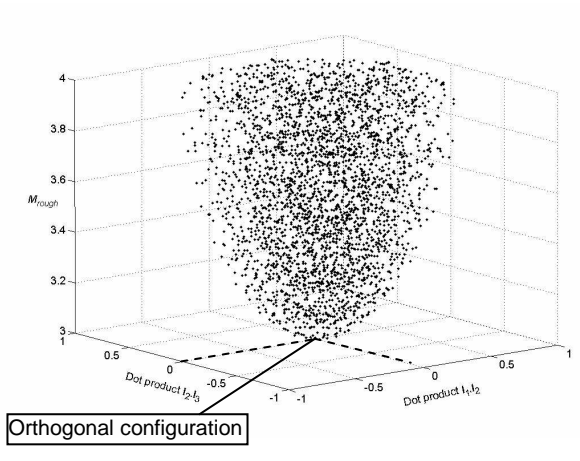


Fig. 8  $M_{rough}$  versus  $l_1, l_2$  and  $l_2, l_3$ .

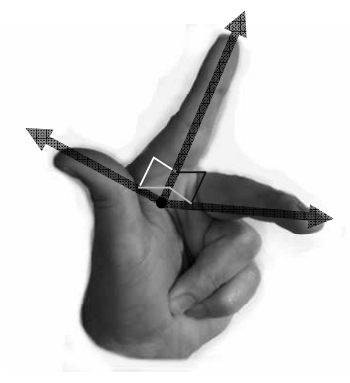


Fig. 9 Representation of orthogonal vectors

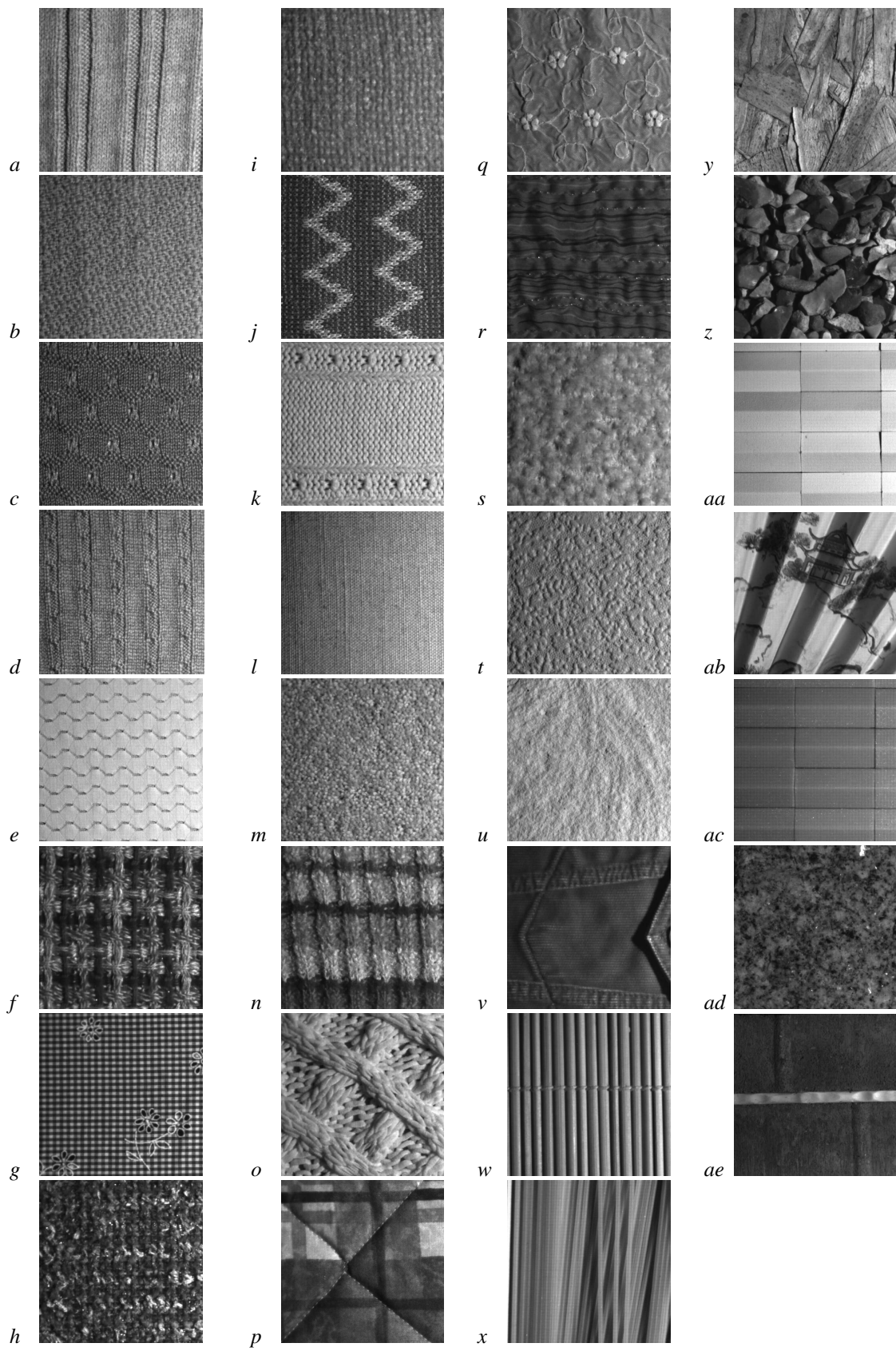


Fig. 10 Sample image of each real texture.

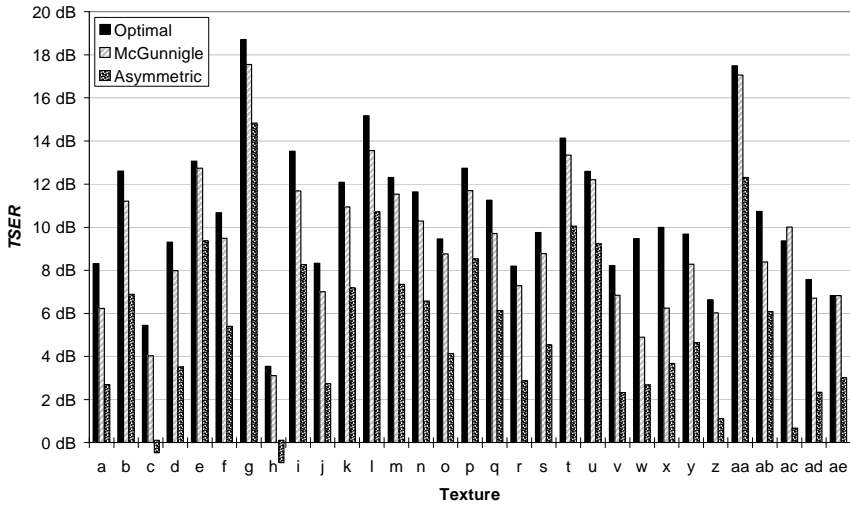
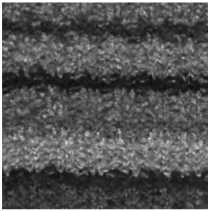


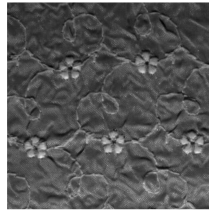
Fig. 11 Practical evaluation of the proposed optimal illumination conditions.

(a) Original image of texture with illumination conditions  $\tau=270^\circ$  and  $\sigma=45^\circ$ .

Texture n

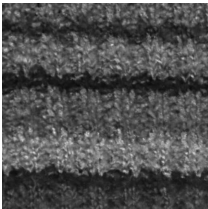


Texture q

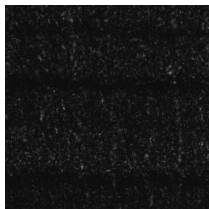


(b) Optimal conditions –  $120^\circ$  spacing with regard to tilt for constant slant.

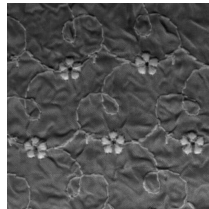
Relit image



Difference image



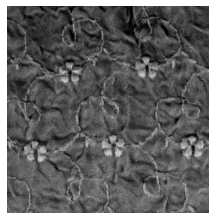
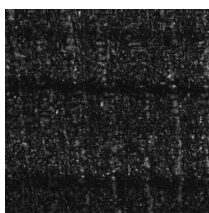
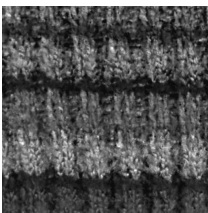
Relit image



Difference image



(c) McGunnigle's scheme –  $90^\circ$  spacing with regard to tilt for constant slant.



(d) Asymmetric arrangement -  $50^\circ$  spacing with regard to tilt for constant slant.

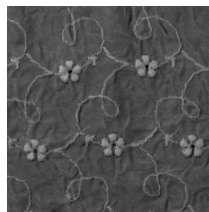
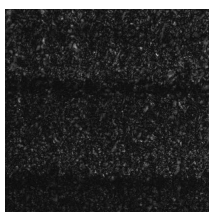
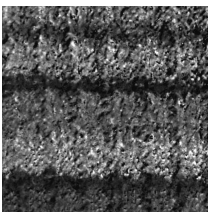


Fig. 12 Comparison of original image with relights for two textures.

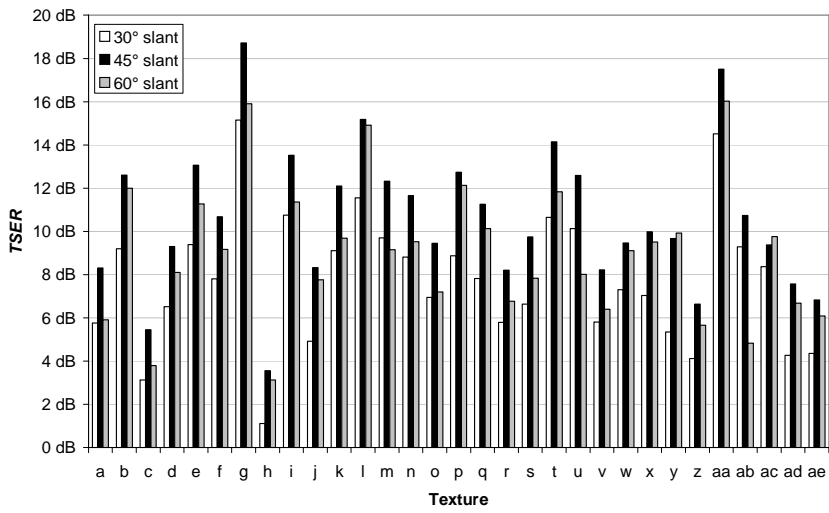


Fig. 13 Practical evaluation of effect of slant angle on accuracy based on optimal illumination configuration with regard to tilt angle ( $\Delta\tau=120^\circ$ ).